Quasi-Direct Drive Actuation for a Lightweight Hip Exoskeleton With High Backdrivability and High Bandwidth

Shuangyue Yu, Tzu-Hao Huang, Xiaolong Yang, Chunhai Jiao, Jianfu Yang, Yue Chen, *Member, IEEE*, Jingang Yi, *Senior Member, IEEE*, and Hao Su, *Member, IEEE*

Abstract—High-performance actuators are crucial to enable mechanical versatility of wearable robots, which are required to be lightweight, highly backdrivable, and with high bandwidth. State-of-the-art actuators, e.g., series elastic actuators, have to compromise bandwidth to improve compliance (i.e., backdrivability). In this article, we describe the design and human–robot interaction modeling of a portable hip exoskeleton based on our custom quasi-direct drive actuation (i.e., a high torque density motor with low ratio gear). We also present a model-based performance benchmark comparison of representative actuators in terms of torque capability, control bandwidth, backdrivability, and force tracking accuracy. This article aims to corroborate the underlying philosophy of "design for control," namely meticulous robot design can simplify control algorithms while ensuring high performance. Following this idea, we create a lightweight bilateral hip exoskeleton to reduce joint loadings during normal activities, including walking and squatting. Experiments indicate that the exoskeleton is able to produce high nominal torque (17.5 Nm), high backdrivability (0.4 Nm backdrive torque), high bandwidth (62.4 Hz), and high control accuracy (1.09 Nm root mean square tracking error, 5.4% of the desired peak torque). Its controller is versatile to assist walking at different speeds and squatting. This article demonstrates performance improvement compared with state-of-the-art exoskeletons.

Index Terms—Exoskeleton, high-torque actuator, human augmentation, quasi-direct drive (QDD) actuation, wearable robots.

Shuangyue Yu, Tzu-Hao Huang, Xiaolong Yang, Chunhai Jiao, Jianfu Yang, and Hao Su are with the Lab of Biomechatronics and Intelligent Robotics (BIRO), Department of Mechanical Engineering,The City University of New York, City College, NY 10023 USA (e-mail: syu003@citymail.cuny.edu; thuang@ccny.cuny.edu; xyang1@ccny.cuny.edu; cjiao000@citymail.cuny.edu; jy2863@columbia.edu; hao.su@ccny.cuny.edu).

Yue Chen is with the Department of Mechanical Engineering, University of Arkansas, Fayetteville, AR 72701 USA (e-mail: yc039@uark.edu).

Jingang Yi is with the Department of Mechanical and Aerospace Engineering, Rutgers, The State University of New Jersey, Piscataway, NJ 08854 USA (e-mail: jgyi@rutgers.edu).

I. INTRODUCTION

SAFE and dynamic interaction with a human is of paramount importance for collaborative robots. State-of-the-art actuators (defined as motors with transmission), e.g., series elastic actuators (SEAs), have to compromise bandwidth to improve compliance (i.e., backdrivability) during interaction with a human. This limitation is particularly prominent for lower-limb wearable robots as it involves repeating high-force interaction with humans during locomotion with disturbance from changing gaits and varying terrain conditions [1]–[3]. Recent exoskeletons focus on advanced algorithms to improve control performance [4]–[9]. However, there is limited work in the actuation hardware design to provide the physical intelligence of robots, which is intrinsic to the system to ensure high performance without relying on complicated algorithms [10]. High-torque density electric motors represent a solution to meet the multifaceted requirements of wearable robots ranging from lightweight, torque, bandwidth, and backdrivability to ensure minimal mass penalty, robustness, and agility for practical applications.

Besides actuators for soft-material robots, there are three primary actuation methods for wearable robots, namely conventional actuation, series elastic actuation, and quasi-direct drive (QDD) actuation (also known as proprioceptive actuation [10], [11]). Conventional actuation uses high-speed and low-torque motors [typically brushless direct current motors (BLdc)] with large ratio gears [12]–[15]. It can meet certain requirements such as assistive torque, angular velocity, and control bandwidth, but suffers from high mechanical impedance (i.e., resistive to human movements). Although control algorithms might be able to ameliorate the undesirable high impedance, it is infeasible to eliminate this side effect due to the inherent high inertia and high friction of actuators. SEAs (including parallel elastic actuators and other variable stiffness elastic actuators) overcome the backdrivability limitation [16]–[19] using the spring-type elastic elements. However, SEAs typically have to sacrifice the performance in control bandwidth, system complexity, system mass, and dimension, resulting in the limited practical benefits for wearable robots. Besides, the advantages of textile-based

soft exosuits [4], [5], [20] (typically around 50:1 gear ratio) primarily originate from the wearable structure (textile) and cable transmission. Thus, textile-based soft exosuits have similar high impedance limitations as SEA.

QDD actuation composed of high torque motors and low gear ratio transmission represents a new solution to achieve versatility for wearable robots, namely high bandwidth and high backdrivability for a wide variety of human activities. QDD actuation is recently studied for legged robots, but portable powered exoskeletons have disparate requirements in terms of mass, torque, and speeds. Wensing *et al.* [10] presented custom motors (interior rotor design, see Section III-A) for cheetah robots, and the motor peak torque is 38.2 at 60 A electrical current. But the 1 Kg motor mass is too bulky and heavy for portable exoskeletons (overall weight of a bilateral exoskeleton with this motor is likely to be around 7 Kg including transmission, wearable structures, and battery). The mini cheetah robot [25] and commercial QDD actuators for quadruped robots have high torque density because of exterior robot design (see Section III-A), but the nominal actuator torque is only 6–7 Nm, which is still not sufficient for lower limb exoskeleton applications. In the exoskeleton community, the authors in [21]–[24] presented tethered exoskeletons following the QDD paradigm and proved its feasibility. However, those systems are tethered and heavy, thus are not practical for real-world applications. Our recent work [25] presented a high-torque density electric motor (0.67 Nm nominal torque) with a low transmission ratio in a portable unilateral knee exoskeleton. The actuator can generate 6 Nm nominal torque and 16 Nm peak torque, and the device weighs 3.2 kg. Our hybrid soft exoskeleton for knee assistance [11] is tethered. Thus, it is not suitable as personal mobility devices for community ambulation. Zhu *et al.* [26] proposed a knee exoskeleton with 2.69 kg unilateral mass using a QDD actuation. The 1.15 kg actuator can generate a 10.6 Nm nominal torque and 20 Nm peak torque. The desire to further improve robot torque density and torque capability, to reduce the weight, and to investigate interaction modeling of this new actuation paradigm for portable exoskeleton devices motivates this article.

This article presents a high-performance QDD actuator using custom high torque density motor and low ratio gear transmission (8:1). The contributions of this article include 1) a design of quasi-direct drive actuation based exoskeleton that demonstrates mechanical versatility for being lightweight (3.4kg overall mass), highly-backdrivable (0.4 Nm backdrive torque) with high nominal torque (17.5 Nm) and high control bandwidth (62.4 Hz), as shown in Fig. 1; 2) a unified human–robot interaction model that captures backdrivability and control bandwidth of three actuation paradigms (i.e., conventional actuator, SEA, QDD actuator) with comprehensive benchmark results; 3) systematic characterization the QDD actuator based hip exoskeleton in terms of output torque capability, control bandwidth, backdrivability, and torque control accuracy performance during walking and squatting assistance. To the best of our knowledge, our hip exoskeleton has the best performance in terms of all key mechanical metrics, including nominal torque, torque density, backdrivability, bandwidth, and accuracy, as benchmarked with state-of-the-art hip exoskeletons [16]–[19] and hip exosuits [4],
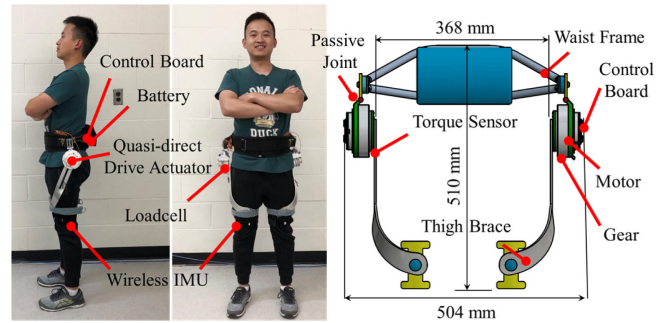

Fig. 1. Hip exoskeleton is versatile in terms of high bandwidth and high backdrivability thanks to its high torque density QDD actuation. The mechanism of the hip exoskeleton is composed of a waist frame, two actuators, tow torque sensors, and two thigh braces. The passive joints allow the wearer's hip joint free abduction and adduction.

[5], [20]. High torque density will lead to reduced mass penalties and enhanced metabolic economy, high backdrivability is crucial for fluid human movements, and high bandwidth is suitable to handle rapid or unexpected human movements. Though the focus of this article is to reduce joint loadings of able-bodied populations for regular activities, our exoskeleton also has the potential to promote the independent living of people with lower-limb impairments.

II. DESIGN REQUIREMENTS

The design of the hip exoskeleton needs to satisfy the kinematics and kinetics requirements. For walking, human hip joints have flexion/extension movements in the sagittal plane and abduction/adduction in the frontal plane. Therefore, the hip joint of the exoskeleton needs to accommodate those two degrees of freedom. For level-ground walking, the range of motion of a human hip joint is 32.2° flexion, 22.5° extension, 7.9° abduction, and adduction 6.4°. We design the robot with a larger range of motion than the standard requirements to handle a heterogeneous population for a wide variety of activities beyond walking. The hip exoskeleton possesses the range of motion 130° flexion, 40° extension, 90° abduction, and 60° adduction, encompassing the maximum range of the human hip joints [26]. Therefore, our hip exoskeleton can assist walking, sitting, squatting, and stair climbing. For a human of 75 kg walking at 1.6 m/s, the peak torque and the speed of the hip joint are 97 Nm (1.3 Nm/Kg) and 2.3 rad/s, respectively [27]. Seo *et al.* [28] and Lee *et al.* [29] show that a hip exoskeleton with 12 Nm torque resulted in 15.5% metabolics reduction for uphill walking. To gain higher torque output, our hip exoskeleton is required to provide 20 Nm torque (about 20% of the biological joint moment). The design requirements are summarized in Table I.

III. QDD ACTUATION

QDD actuation [10], [30] is a new paradigm of robot actuation design that leverages high torque density motors with a low ratio transmission mechanism. It is recently studied for legged robots [10] and wearable robots [31], [32] have the benefits including

TABLE I
DESIGN PARAMETERS OF THE HIP EXOSKELETON

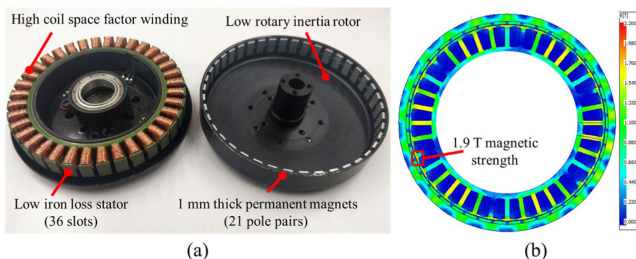| Parameters	Walking	Desired	Actual
Hip flexion/extension (°)	32.2/22.5	32.2/22.5	130/40
Hip abduction/adduction (°)	7.9 /6.4	7.9 /6.4	90/60
Max hip joint moment (Nm)	97	19.4	20
Max hip joint speed (rad/s)	2.3	3	19.6
Exoskeleton weight (kg)	——	5	3.4

Fig. 2. (a) Custom-designed pancake exterior rotor type and concentrated winding BLdc electric motor. The fractional slot design (36 slots, 21 pole pairs) reduces cogging torque and minimizes copper loss [31]. (b) By using sintered NdFeB permanent magnets, the finite element analysis simulation result shows under no current in the winding condition, the magnetic strength of the stator can reach 1.9 T.

a simplified mechanical structure, reduced mechanical inertia, and embodied physical intelligence (high backdrivability and high bandwidth without relying on active control) to improve safety and robustness in unstructured environments.

Due to the low gear ratio transmission, the primary limitation of the QDD actuation paradigm is the output torque density. To overcome this barrier, a custom QDD actuator is developed that provides high nominal torque, well-integrated, reduced speed (than conventional high-speed motors but fast enough for human movement assistance), and high torque-inertia ratio.

A. High Torque Density Motor

In terms of topology, Reichert *et al.* [33] and Lee *et al.* [34] show that the exterior rotor and concentrated winding type BLdc electric motor has higher torque density. Besides topology design, we perform both mechanical and electromagnetic optimization to further improve its performance. As shown in Fig. 2(a), the custom motor uses fractional-slot type winding, which reduces the cogging torque to 25 ± 12.5 mNm. Compared with commercially available motors (Maxon EC90, 12 pole pairs [17]) and research prototypes (ten pole pairs and 18 rotor slots [31]), our design has 21 pole pairs and 36 rotor slots which have higher output torque capability and lower cogging torque. The copper loss is 32.6 W, which is 26% less than the research prototypes (44.3 W) [31].

Our motor winding is attached to the stators, and the rotor only consists of 1-mm thick permanent magnet chips and the rotor cover. The lightweight exterior rotor reduces rotary inertia and increases the torque-inertia ratio. Moreover, the customized motor uses sintered Neodymium-Iron-Boron (NdFeB) permanent magnets, which can reach 1.9 T magnetic field intensity, as shown in Fig. 2(b).

TABLE II
PARAMETERS IN HUMAN-EXOSKELETON COUPLED MODEL

Parameter	Unit	Conventional	SEA	QDD
Motor	-	EC 45	EC 90	Ours
Nominal voltage	V	24	48	42
Nominal current	A	3.21	2.27	7.5
Nominal Torque	Nm	0.128	0.533	2.165
Motor resistance	Ω	0.608	2.28	0.58
Motor inductance	mH	0.46	2.5	0.21
Motor friction coefficient	Nm·s/rad	0.01	0.01	0.08
Torque constant	Nm/A	0.0369	0.217	0.2886
Motor inertia	g·cm^2	181	3060	895
Gear ratio	-	50:1	100:1	8:1
Transmission stiffness	Nm /rad	500	120	500
Transmission damping	Nm·s/rad	0.01	0.01	0.01

TABLE III
COMPARISON OF HIP EXOSKELETONS PERFORMANCE
OF THREE ACTUATION PARADIGMS

Parameter	Unit	Conventional [13]	SEA [17]	QDD (this work)
Output nominal torque	Nm	8	40	17.5
Actuator mass	kg	~0.50	1.80	0.77
Actuator nominal torque density	Nm/kg	16	22.2	20.7
Control bandwidth	Hz	5.1	4.2	73.3
Backdrive torque	Nm	2.88	6.10	0.97

The customized high torque density motor weighs 274 g with 0.9 kg·cm^2 rotor inertia and can generate about 2.165 Nm nominal torque. This results in 8 Nm/kg nominal motor torque density and 2.2 Nm/ kg·cm^2 torque-inertia ratio. Compared with the benchmark motor (Maxon EC flat 505592, 0.7 Nm/kg nominal torque density, 0.14 Nm/ kg·cm^2 torque-inertia ratio) [17], our customized motor has about 11 times higher torque density and about 16 times higher torque-inertia ratio. The detailed specifications of the motor can be found in Tables II and III.

B. QDD Actuator

To meet the dimension and mass requirements of exoskeleton design, a fully-integrated actuator can reduce mass, dimension, and ensure operation safety. This is crucial to overcome the barriers for widespread adoption of wearable robots [35], [36] that have been typically considered heavy and bulky. We develop a compact direct-drive actuator with fully-integrated components, as shown in Fig. 3 using the custom-designed motor.

The overall actuator weight is 777 g, and it includes a high torque density motor, an 8:1 ratio planetary gear, a 14 bits high accuracy magnetic encoder, and a 10–60 V wide range input motor driver and controller. Moreover, the low-level control loop is implemented in the driver-control electronics to realize low-level control, including position, velocity, and current control. High-level control devices can send a command to read and write the real-time information actuator through the controller area network (CAN bus) communication protocol. With a nominal voltage of 42 V, the actuator reaches a nominal speed of 188
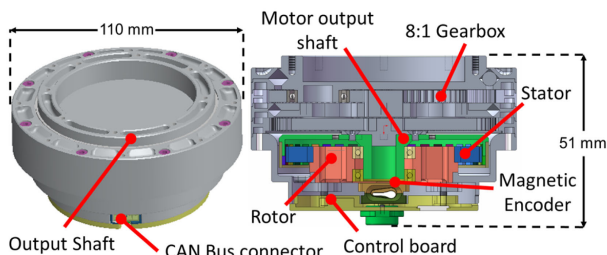
Fig. 3. Fully-integrated QDD actuator consists of a high torque density motor, an 8:1 gearbox, a magnetic encoder, and control electronics. The motor is designed to be compact ($\Phi 110 \times 52$ mm^2 height), lightweight (777 g), and able to generate high torque (17.5 Nm nominal torque and 42 Nm peak torque).

Fig. 4. Demonstration of the range of motion of the robot. The hip exoskeleton is designed with a wide range of motion to support the wearer to perform various activities.

RPM (19.7 rad/s). Thanks to the QDD design using low gear ratio transmission, the actuator has low output inertia (57.6 kg·cm^2), which is essential to render low impedance to minimize the resistance to natural human movements.

IV. Design and Modeling of QDD Exoskeleton

This section presents the mechanical and electrical design of the exoskeleton, modeling of human–robot interaction, and analysis of mechanical versatility. Our QDD actuation robot is benchmarked with conventional actuation and SEAs to realize minimal resistance to human movements and high dynamic performance to understand human–robot interaction.

A. High Backdrivability and High-Bandwidth Exoskeleton

Since sagittal plane movements produce the dominant positive power of hip joints during walking and squatting, the robot is designed to have one active degree of freedom (DOF) and passive DOFs in frontal and transverse planes to ensure a natural range of motion. The hinge joints that connect the motor housings and the waist frame enable passive DOF in the frontal plane (i.e., abduction and adduction). The elastic thigh straps enable passive DOF in the transverse plane (i.e., internal/external rotations). The mechanical system of the hip exoskeleton is mainly composed of a waist frame, two actuators, two torque sensors, and two thigh braces, as shown in Fig. 1. The robot is symmetric about the sagittal plane. We design a waist frame to anchor the two actuators. The curvature of the waist frame is conformal to the wearer's pelvis, enabling uniform force distribution on the human body. A wide waist belt is chosen to attach the waist frame to the user, aiming to maximize the contact area and reduce pressure on the human. The two motors are fixed to the waist frame by the motor housings. The two actuators work in the sagittal plane to assist the flexion and extension of the hip joints. A custom torque sensor (± 40 Nm full scale and ± 0.1 Nm resolution) is assembled to the output flange of the actuator to measure output torque, as shown in Fig. 1. The thigh brace is connected to the medial side of the torque sensor and transmits the actuator torque to the wearer's thigh. This curved structure of the thigh brace enables the assistive force on the wearer's thigh to be perpendicular to the frontal plane on the centerline of the thigh. The wearer does not suffer from the shear forces, which typically induce discomfort. Since hip extension moment
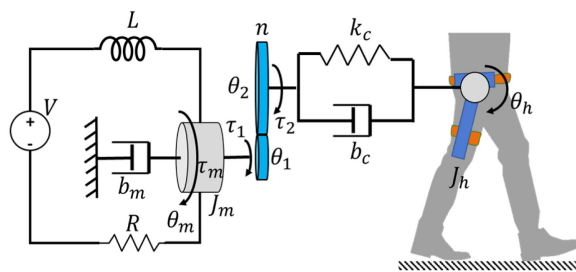

Fig. 5. Human-exoskeleton coupled dynamic model. It consists of four modules: motor system, speed reduction mechanism, transmission, wearable structure, and human leg. V: motor nominal voltage; R: motor resistance (phase to phase); L: motor inductance (phase to phase); b_m: motor friction coefficient; τ_m: torque developed by the motor; θ_m: motor rotation angle; J_m: motor inertia; τ_1: motor output torque; θ_1: motor rotation angle before the gear reduction; n: gear ratio; τ_2: gearbox output torque; θ_2: gearbox output rotation angle; k_c: transmission stiffness; b_c: transmission damping; and J_h: human leg inertia.

is slightly larger than flexion moment during walking, the metallic thigh brace is used to generate extension assistance (see Figs. 1 and 4). To reduce the loss of moment transmission while ensuring a comfortable human-exoskeleton contact, we used non-extensible fabric straps with foam for flexion assistance. Our hip exoskeleton supports the wearer to perform normal activities that require a wide range of motion, including stair climbing, sit-to-stand, and squatting, as shown in Fig. 4.

The electrical system of the hip exoskeleton supports high-level torque control, motor control, sensor signal conditioning, data communication, and power management. The local motor controller is developed based on a motor driver and a DSP microcontroller to measure the motor motion status and realize motor current, velocity, and position control. The high-level microcontroller runs on Arduino Due to torque control. It acquires a lower-limb attitude from the wireless inertial measurement unit (IMU) sensors and conditions torque signals from the custom loadcells in real-time.

B. Human-Exoskeleton Coupled Dynamic Model

In this section, QDD and the human-exoskeleton interaction is modeled in comparison with series elastic actuation to understand the interaction dynamics by characterizing the mechanical versatility of the robot in terms of backdrivability, control bandwidth, and torque capability as shown in Fig. 5. The

system can be approximated as a mechanical system consisting of a motor, a gearbox, transmission, and wearable structures attached to the human hip joint. The connections between these modules are modeled as springs and dampers to represent the force and motion transmission.

The motor generates the torque τ_m with an input voltage V. The dynamics of the motor electrical system can be characterized by the winding resistance R and inductance L. The motor torque τ_m is generated by current i and the torque constant of motor is k_t. The back-electromagnetic force V_b is proportional to the motor velocity $\dot{\theta}_m$ and the constant of back-electromagnetic force is k_b. The governing equation of the motor electrical system is

$$V - V_b = L\frac{d\dot{i}}{dt} + Ri \tag{1}$$

$$\tau_m = k_t i \tag{2}$$

$$V_b = k_b \dot{\theta}_m. \tag{3}$$

Meanwhile, the damping coefficient of viscous friction from the rotor is denoted by b_m. The torque applied to the input shaft before the gear reduction is τ_1. The motor governing equation

$$\tau_m = J_m \ddot{\theta}_m + b_m \dot{\theta}_m + \tau_1 \tag{4}$$

where J_m denotes the moment of inertia of the motor rotor around its rotation axis and θ_m denotes the motor angle.

The motor outputs the torque τ_1 to the input shaft of the gearbox with a gear ratio $n\!:\!1$. The output angle is reduced, and the torque is amplified through the gearbox

$$\theta_1 = \theta_m, \ \theta_2 = \frac{\theta_1}{n}, \ \tau_2 = n\tau_1. \tag{5}$$

In (5), θ_1 and θ_2 denote the rotation angle of the input shaft and output shaft in the gearbox, respectively, and τ_1 and τ_2 denote the torque applied on the input shaft and output shaft, respectively.

The transmission of the exoskeleton can be designed with rigid linkages, spring, cable-pulley systems, cable-textile systems which can be modeled as a transmission stiffness and damping, denoted by k_c and b_c, respectively

$$\tau_2 = b_c s\left(\dot{\theta}_2 - \dot{\theta}_h\right) + k_c\left(\theta_2 - \theta_h\right). \tag{6}$$

The human thigh is governed by the equation

$$J_t \ddot{\theta}_h + b_c s\left(\dot{\theta}_h - \dot{\theta}_2\right) + k_c\left(\theta_h - \theta_2\right) = \tau_l \tag{7}$$

where J_t is the inertia of the thigh orthosis and human limb. θ_h is the hip rotation angle. τ_l is the human torque generated by the muscles. τ_a is the torque applied on the human thigh can be calculated as (8), and τ_a can be assistive torque or resistive torque

$$\tau_a = \tau_2 = b_c s\left(\frac{\dot{\theta}_m}{n} - \dot{\theta}_h\right) + k_c\left(\frac{\theta_m}{n} - \theta_h\right). \tag{8}$$

Let s be the Laplace variable, and the system block diagram can be modeled as Fig. 6.
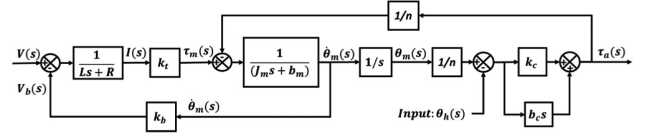

Fig. 6. Block diagram of human-exoskeleton open loop system.

Assuming the initial condition $\theta_h(0), \dot{\theta}_h(0)$, and $V(0)$ is equal to zero and neglect the inductance L due to its small value [37]. The Laplace transform of assistive torque $T_a(s)$ is related to the Laplace transform of the hip rotation angle $\theta_h(s)$ and input voltage $V(s)$, shown as follows:

$$\tau_a(s) = n_1(s)\left[\frac{n_2(s)}{d(s)}V(s) + \frac{n_3(s)}{d(s)}\theta_h(s)\right]$$

$$= G_1(s)V(s) + G_2(s)\theta_h(s)$$

$$d(s) = J_e s^2 + b_e s + k_e$$

$$J_e = n^2 J_m R, \ b_e = n^2 R b_m + n^2 k_b k_t + R b_c, \ k_e = R k_c$$

$$n_1(s) = (b_c s + k_c); \ n_2(s) = n k_t$$

$$n_3(s) = -n^2\left[J_m R s^2 + (R b_m + k_b k_t)s\right]. \tag{9}$$

$G_1(s)$ is the transfer function that defines the relationship between the voltage input $V(s)$ and human–robot interaction torque $\tau_a(s)$

$$G_1(s)\,|_{\theta_h(s)=0} = \frac{\tau_a(s)}{V(s)} = \frac{n_1(s)n_2(s)}{d(s)}. \tag{10}$$

$G_2(s)$ is the transfer function that defines the relationship between the human motion input $\theta_h(s)$ and human–robot interaction torque $\tau_a(s)$

$$G_2(s)\,|_{V(s)=0} = \frac{\tau_a(s)}{\theta_h(s)} = \frac{n_1(s)n_3(s)}{d(s)}. \tag{11}$$

The natural frequency ω_n of the open-loop torque control for the second-order system is

$$\omega_n = \sqrt{\frac{k_e}{J_e}} = \sqrt{\frac{R k_c}{n^2 J_m R}} = \sqrt{\frac{k_c}{n^2 J_m}}. \tag{12}$$

The effective moment of inertia J_e is equal to $n^2 J_m$ and the natural frequency ω_n of the open-loop torque control is directly modulated by gear ratio n and the transmission stiffness k_c and moment of inertia of the motor J_m. In [12], it also concluded that the reflected actuator inertia directly modulates the effective mass, and small reflective actuator inertia will increase the open-loop force control bandwidth. The smaller gear ratio, the smaller movement of inertia of the motor, and the larger transmission stiffness will generate higher natural frequency.

To investigate the backdrivability, $V(s)$ is set to zero to identify the property of the passive mechanism, and the output resistive torque and output link impedance are used to analyze the back drivability. The resistive torque τ_a induced by the human motion $\theta_h(s)$ can be derived through (13). The output

link impedance is derived as (14)

$$\tau_a\left(s\right) = G_2\left(s\right)\theta_h\left(s\right)$$
$$= \frac{-\left(b_c s + k_c\right)n^2\left[J_m R s^2 + \left(R b_m + k_b k_t\right)s\right]}{n^2\left[J_m R s^2 + \left(R b_m + k_b k_t\right)s\right] + R b_c s + R k_c}\theta_h\left(s\right)$$
$$(13)$$

$$Z_o\left(s\right) = \frac{\tau_a\left(s\right)}{\dot\theta_h\left(s\right)} = \frac{\tau_a\left(s\right)}{s\theta_h\left(s\right)}. \quad (14)$$

As the gear ratio is sufficiently small, the resistive torque can be approximated as zero, shown as follows:

$$\lim_{n\to 0}\tau_a\left(s\right) = 0. \quad (15)$$

As the gear ratio is large, the resistive torque will be approximated to (16) and the transmission damping constant b_c and stiffness constant k_c are the dominated terms

$$\lim_{n\to\infty}\tau_a\left(s\right) \approx -\left(b_c s + k_c\right)\theta_h\left(s\right). \quad (16)$$

When the gear ratio is 1, the resistive torque is shown in (17), and we can observe the resistive torque is modulated by the gear ratio n, the transmission damping constant b_c, the transmission stiffness constant k_c, the motor inertia J_m, the motor damping constant b_m, the motor resistance R, the motor torque constant k_t, and the back EMF constant k_b

$$\tau_a\left(s\right)|_{n=1} = -\frac{\left(b_c s + k_c\right)\left(J_m R s^2 + R b_m s + k_b k_t s\right)}{J_m R s^2 + \left(R b_m + k_b k_t + R b_c\right)s + R k_c}\theta_h\left(s\right). \quad (17)$$

Through (15)–(17), a highly backdrivable mechanism, low output link impedance, and low resistive torque can be achieved by a smaller gear ratio n, a smaller damping constant b_c, or a smaller stiffness constant k_c.

C. Actuation Paradigm Based Hip Exoskeleton Benchmark

Based on the human–robot interaction model, we benchmark the performance of state-of-the-art hip exoskeletons in terms of actuation paradigms, including conventional actuation, SEA, and QDD. The difference between conventional actuation and SEA is the transmission stiffness. The difference between the QDD and conventional actuation is the gear ratio and the motor type. The representative devices include 1) the conventional actuation based hip exoskeleton [13]; 2) the SEA-based hip exoskeleton [17]; 3) our QDD hip exoskeleton. Table II shows the key parameters of the actuators from these three representative hip exoskeletons. Note that the parameters that affect the backdrivability vary within a specific range [10], [38]. For simplicity of benchmark comparison, we set the transmission damping constant of 0.01 Nm·s/rad in the simulation model and use a large transmission stiffness of 500 Nm/rad for the conventional and QDD actuators, and set a relatively small transmission stiffness (i.e., 120 Nm/rad) for the SEA due to its spring component.

To benchmark the versatility of three actuation methods, we use resistive torque (backdrivability) and bandwidth of torque
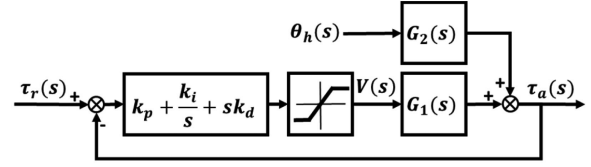

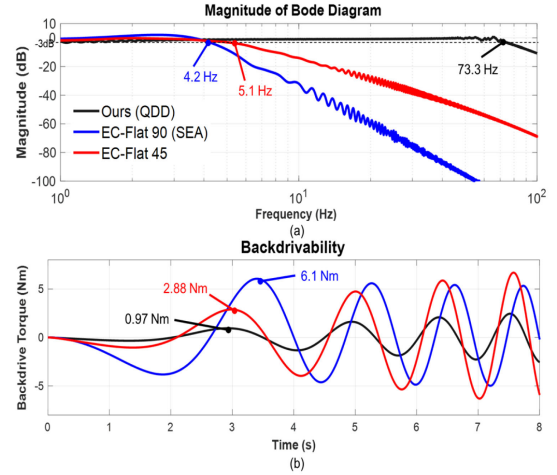Fig. 7. Block diagram of closed-loop torque control in the human-exoskeleton system.

Fig. 8. Bandwidth and backdrivability simulation result based on the human–robot interaction model. The result shows that our QDD actuator has a theoretical 73.3 Hz bandwidth and 0.97 Nm backdrivability. Compared with the other two actuation paradigms, the QDD actuation demonstrates significant improvements in terms of bandwidth and backdrivability.

control as metrics to demonstrate the benefit of low gear ratio and high torque density motor and the results are as shown in Fig. 7. To approximate the real condition, the Simulink model used the saturation function to limit the maximum voltage. The maximum voltage of conventional actuation, SEA, and QDD is set as 24V, 48V, and 42V, respectively.

For the bandwidth analysis of the closed-loop torque control, the block diagram is shown in Fig. 6, where the input reference torque is a chirp signal (0∼100 Hz) with 5 Nm magnitude, and the input human hip angle is set as zero (simulation for the fixed output link).

For the resistive torque simulation (i.e., backdrivability), the block diagram is shown in Fig. 7 and the input human hip angle is set as a chirp signal (0∼1 Hz) with 10° magnitude, and the voltage source V(s) is set as zero. The simulation results (see Fig. 8) demonstrate that the designed QDD actuation with lower gear ratio and high torque density motor achieves mechanical versatility in terms of high bandwidth (73.3 Hz) and high backdrivability (backdrive torque 0.97 Nm). Both the conventional actuation and SEA have compromised bandwidth or backdrivability.

In addition to those two metrics, a high-performance portable hip exoskeleton also requires high torque output and low mass. In Table III, we listed the comparison results of these three actuators' performance. The key factors in evaluating the actuator performance are torque inertia ratio, bandwidth, backdrivability,
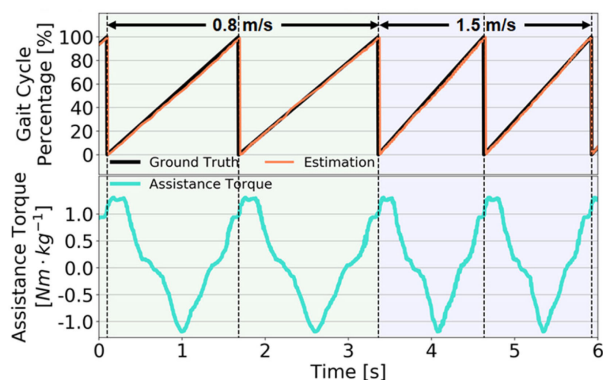
Fig. 9. (Top) Orange line represents the estimated gait cycle percentage by our regression method, whereas the black line represents the ground truth calculated offline by insole signals. The robust gait estimation is able to compensate for the disturbance due to walking speed changes. The estimated gait matches well with the ground truth ($R^2 = 0.997$). (Bottom) Turquoise line shows 100% of the biological torque generated by our algorithm.
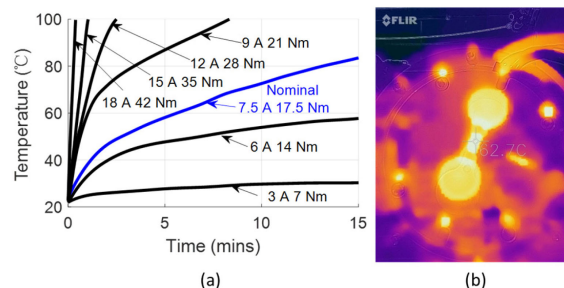

Fig. 10. (a) Stator temperature over time for different current conditions. (b) Thermal image after 15 min of continuous 7.5 A current operation. The actuator surface reached the maximum temperature of 62.7 °C.

and output torque density. It shows that our QDD actuator not only outperforms in terms of bandwidth and backdrivability, it also possesses a significantly higher torque inertia ratio without sacrificing torque density as its two counterparts (high gear ratio can easily enhance torque).

Due to the simplification of the model and variability of parameters (e.g., human limb inertia), the simulation results may deviate from the actual values. Though the SEAs model presented in this simulation may not represent novel methods of SEAs [18], [19] (e.g., we can use those novel methods of SEAs for QDD actuation too), our analysis is able to capture the underlying characteristics of the three actuation paradigms.

V. CONTROL STRATEGIES

The control system is based on a hierarchical architecture composed of a high-level control layer that robustly detects gait intention to compensate for the uncertainty due to varying walking and squatting speed (see Fig. 9), a middle-level control that generates assistance torque profile (see Fig. 9), and a low-level control layer that implements a current-based torque control.

To compensate for the uncertainties caused by changing gait speeds, an algorithm recently developed in our lab that uses a data-driven method [39] with a neural network regressor to estimate the walking and squatting percentage in real-time by the signals from two IMUs. These two IMUs are mounted on anterior of both left and right thighs (see Fig. 1). These sensors provide the motion information, including Euler angle, angular velocity, and acceleration at a frequency of 200 Hz. Each signal channel is scaled to have zero mean and unit variance. The motion information during the last 0.4 s sliding time window constitutes the input vector of the neural network for both offline training process and online control. The neural network used in this algorithm has one hidden layer with 30 neurons as well as a sigmoid activation function and deploys the Xavier initialization of network weights. We collect the walking and squatting data from three able-bodied subjects at several different speeds, and our algorithm could achieve an $R^2 = 0.997$ on the test set.

After obtaining the gait percentage, the middle-level controller calculates the assistive torque according to a predefined torque profile expressed as a look-up table. The predefined torque profile for walking is generated by the human biological model in [40], and squatting is a sine wave. Searching the gait percentage in the look-up table and applying an interpolation calculation could produce the desired assistance torque.

The low-level torque control architecture is composed of an inner-loop control and an outer-loop control. The inner loop implements motor current control in the local motor controller. The outer loop implements the torque control in Arduino Due whose feedback signal is from motors, loadcells, and IMU-based gait detection. The simplicity of the control algorithm corroborates the underlying philosophy about "design for control," namely robots can be designed to simplify the control while ensuring high performance.

VI. EXPERIMENTAL RESULTS

To demonstrate the backdrivability and bandwidth of the hip exoskeleton, we conducted five experiments on the actuator and the hip exoskeleton to systematically characterize the mechanical versatility of the device.

A. Motor Nominal Current Evaluation

The actuator output capability is highly limited by the motor's winding temperature. To evaluate the actuator working current performance, we operated the actuator continuously in the stall mode under different output currents. The stator temperature was measured by an embedded temperature sensor, and the actuator surface temperature was measured by a portable FLIR thermal camera. The experiment was performed in a 22 °C lab environment without external heat dissipation. The maximum operating time was set to 15 min and the maximum temperature of the stator to 100 °C. Fig. 10(a) shows the stator temperature changes with time under different current conditions. Fig. 10(b) shows the thermal camera image for 15 min when the actuator stalls under the nominal current and the highest temperature of the actuator shell is 62.7 °C. The experiment demonstrates that the custom actuator is able to produce a nominal torque of 17.5 Nm under 7.5 A nominal current and about 42 Nm peak torque under 18 A current based on the calibrated torque constant.
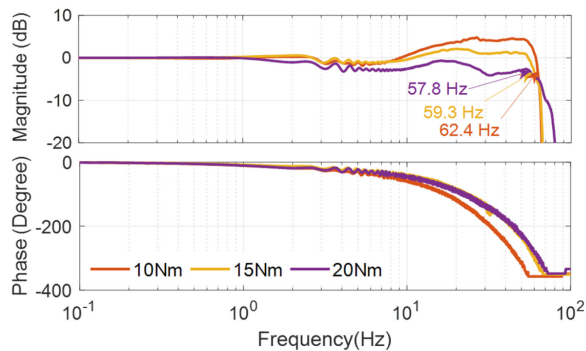
Fig. 11. Bode plot for 10 Nm, 15 Nm, and 20 Nm torque control. The high bandwidth (highest value is 62.4 Hz) demonstrates the ability to handle high-frequency movements of humans in comparison with state-of-the-art results (for instance, a 5 Hz bandwidth is reported in [16]).
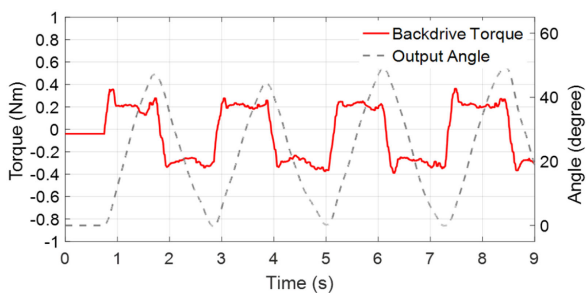

Fig. 12. Backdrivability of the hip exoskeleton in the unpowered mode. The maximum torque of the mechanical resistance is approximately 0.4 Nm in comparison with state-of-the-art results in [16] with 2 Nm and [31] with about 1 Nm.
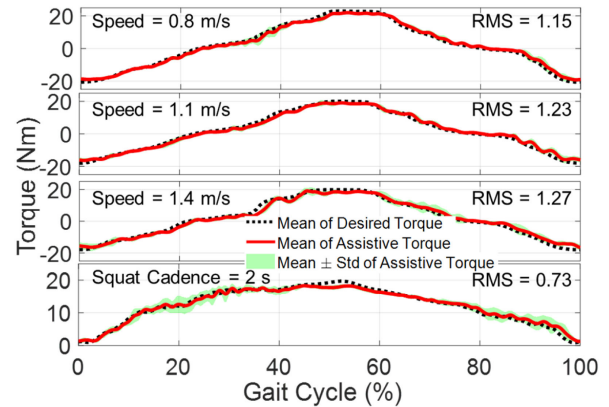

Fig. 13. Torque tracking performance of ±20 Nm assistance during walking and squatting tests. The mean of actual assistive torque (red) tracked the desired torque (black dash) well. The RMS errors of torque tracking (0.8 m/s, 1.1 m/s, and 1.4 m/s walking, 2 s cadence squatting) were 1.15 Nm, 1.23 Nm, 1.27 Nm, and 0.73 Nm, respectively, (5.75%, 6.15%, 6.35%, and 3.65% of the peak torque). The tracking accuracy is superior to the SEA-based exoskeleton (±10 Nm and 21.5% error) [16].

B. Exoskeleton Bandwidth Evaluation

The bandwidth experiment of the torque control was carried out to obtain the Bode plot. A chirp signal was used as the reference torque whose magnitudes are set as 10, 15, and 20 Nm. The Bode plot shows the bandwidth was 57.8, 59.3, and 62.4 Hz, respectively, as shown in Fig. 11. Compared with the model-based control bandwidth (73.3 Hz) simulation results in Fig. 8, the bandwidth obtained through experimental results is slightly low (62.4 Hz). This is primarily due to lower damping and to the effect of the actuator backlash in the hardware prototype. The control bandwidth is much higher than the requirement of human walking, but this is useful for agile human activities, e.g., running and balance control to unexpected external disturbance. Compared with the exoskeletons using SEA [16] with 5 Hz bandwidth, the high control bandwidth robot is safer and more robust to uncertainties.

C. Exoskeleton Backdrive Torque Evaluation

To demonstrate the backdrivability of the exoskeleton, we tested the backdrive torque in unpowered mode. One able-bodied subject wore the exoskeleton, and the hip joint moved with a 32.2° range of motion at 1 Hz while the actuator OFF. The measured rotation angle and the backdrive torque are presented in Fig. 12. The hip exoskeleton has a very low backdrive torque (~0.4 Nm), which shows better backdrivability than SEA and QDD based exoskeletons [16], [31].

D. Torque Tracking for Walking and Squatting Assistance

An able-bodied subject (26-year-old male, 70 kg) wore the hip exoskeleton and walked on a treadmill with the speed varying from 0.8 to 1.4 m/s and squatted on the ground with 2 s cadence. The predefined amplitude of the torque density is 1.3 Nm/kg, resulting in a total of 91 Nm. The control test with 22% of biological hip joint movement during walking and squatting was performed to investigate the tracking performance. The torque of the proposed device (about 20 Nm) is higher than the hip device (12 Nm torque) [13].

A total of 15 tests for the same torque profile for each of the walking and squatting motions were performed. Torque profile, according to the gait cycle, was generated from the high-level controller, and the tracking performance of the hip assistance is shown in Fig. 13. The average RMS error between the desired and actual torque trajectory in 60 tests is 1.09 Nm (5.4% error of the maximum desired torque). The results indicate that the torque controller can follow the torque profile with high accuracy to assist human walking and squatting.

VII. CONCLUSION

This article presents a QDD actuation that is composed of custom high torque density motor and low ratio gear transmission (8:1). It can generate high torque (17.5 Nm nominal torque, 42 Nm peak torque) and weighs 777g. A lightweight bilateral portable hip exoskeleton is developed based on this actuation paradigm, which exhibits mechanical versatility through its high backdrivability (unpowered mode 0.4 Nm backdrive torque) and high bandwidth (62.4 Hz) without using complicated control methods. Both benchmark simulation and experimental study indicate that our exoskeleton with this novel actuation method outperforms state-of-the-art performance [16]–[20] in terms of device mass, bandwidth, backdrivability, and torque tracking performance. This mechanical versatility has the potential to ensure fluid human motion (thanks to high backdrivability), handle rapid or unexpected human movements (thanks to high

bandwidth), and enhance the metabolic economy (thanks to high torque density) in real-world scenarios.

The limitation of this work is that there is no human performance study as it focuses on the quantitative characterization of the QDD actuation for exoskeletons. We will study human performance (e.g., kinetics and electromyography) in our future work. We believe that our enabling technologies and modeling framework offer essential tools to understand human–robot interaction and push the limits to improve locomotion economy [5] as personal mobility assistance devices.

ACKNOWLEDGMENT

REFERENCES

[1] S. Crea *et al.*, "Controlling a robotic hip exoskeleton with noncontact capacitive sensors," *IEEE/ASME Trans. Mechatronics*, vol. 24, no. 5, pp. 2227–2235, Oct. 2019.

[2] T. G. Sugar, E. Fernandez, D. Kinney, K. W. Hollander, and S. Redkar, "HeSA, hip exoskeleton for superior assistance," in *Wearable Robotics: Challenges and Trends*, Berlin, Germany: Springer, 2017, pp. 319–323.

[3] L. M. Mooney and H. M. Herr, "Biomechanical walking mechanisms underlying the metabolic reduction caused by an autonomous exoskeleton," *J. Neuroengineering Rehabil.*, vol. 13, no. 1, pp. 4–15, 2016.

[4] Y. Ding, M. Kim, S. Kuindersma, and C. J. Walsh, "Human-in-the-loop optimization of hip assistance with a soft exosuit during walking," *Sci. Robot.*, vol. 3, no. 15, 2018, Art. no. eaar5438.

[5] J. Kim *et al.*, "Reducing the metabolic rate of walking and running with a versatile, portable exosuit," *Science*, vol. 365, no. 6454, pp. 668–672, 2019.

[6] E. Martini *et al.*, "Gait training using a robotic hip exoskeleton improves metabolic gait efficiency in the elderly," *Sci. Rep.*, vol. 9, no. 1, 2019, Art. no. 7157.

[7] B. Chen, L. Grazi, F. Lanotte, N. Vitiello, and S. Crea, "A real-time lift detection strategy for a hip exoskeleton," *Frontiers Neurorobotics*, vol. 12, pp. 17–27, 2018.

[8] F. L. Haufe *et al.*, "User-driven walking assistance: First experimental results using the myosuit," in *Proc. IEEE 16th Int. Conf. Rehabil. Robot.*, 2019, pp. 944–949.

[9] A. Martínez, B. Lawson, and M. Goldfarb, "A controller for guiding leg movement during overground walking with a lower limb exoskeleton," *IEEE Trans. Robot.*, vol. 34, no. 1, pp. 183–193, Feb. 2018.

[10] P. M. Wensing, A. Wang, S. Seok, D. Otten, J. Lang, and S. Kim, "Proprioceptive actuator design in the MIT cheetah: Impact mitigation and high-bandwidth physical interaction for dynamic legged robots,", *IEEE Trans. Robot.*, vol. 33, no. 3, pp. 509–522, Jun. 2017.

[11] S. Yu, T. Huang, and H. Su, "Design and control of a high-torque and highly-backdrivable hybrid soft exoskeleton for knee injury prevention during squatting," *IEEE Robot. Autom. Lett.*, vol. 4, no. 4, pp. 4579–4586, Oct. 2019.

[12] J. L. Contreras-Vidal *et al.*, "Powered exoskeletons for bipedal locomotion after spinal cord injury," *J. Neural Eng.*, vol. 13, no. 3, 2016, Art. no. 031001.

[13] Y. Lee *et al.*, "A flexible exoskeleton for hip assistance," in *Proc. IEEE/RSJ Int. Conf. Intell. Robots Syst.*, 2017, pp. 1058–1063.

[14] Z. F. Lerner, D. L. Damiano, and T. C. Bulea, "A lower-extremity exoskeleton improves knee extension in children with crouch gait from cerebral palsy," *Sci. Translational Med.*, vol. 9, no. 404, 2017, Art. no. eaam9145.

[15] T. Lenzi, M. C. Carrozza, and S. K. Agrawal, "Powered hip exoskeletons can reduce the user's hip and ankle muscle activations during walking," *IEEE Trans. Neural Syst. Rehabil. Eng.*, vol. 21, no. 6, pp. 938–948, Nov. 2013.

[16] I. Kang, H. Hsu, and A. Young, "The effect of hip assistance levels on human energetic cost using robotic hip exoskeletons," *IEEE Robot. Autom. Lett.*, vol. 4, no. 2, pp. 430–437, Apr. 2019.

[17] T. Zhang and H. Huang, "A lower-back robotic exoskeleton: Industrial handling augmentation used to provide spinal support," *IEEE Robot. Autom. Mag.*, vol. 25, no. 2, pp. 95–106, Jun. 2018.

[18] X. Li, Y. Pan, G. Chen, and H. Yu, "Multi-modal control scheme for rehabilitation robotic exoskeletons," *Int. J. Robot. Res.*, vol. 36, no. 5-7, pp. 759–777, 2017.

[19] N. Paine, S. Oh, and L. Sentis, "Design and control considerations for high-performance series elastic actuators," *IEEE/ASME Trans. Mechatronics*, vol. 19, no. 3, pp. 1080–1091, Jun. 2014.

[20] A. T. Asbeck, K. Schmidt, and C. J. Walsh, "Soft exosuit for hip assistance," *Robot. Auton. Syst.*, vol. 73, pp. 102–110, 2015.

[21] J. S. Sulzer, R. A. Roiz, M. A. Peshkin, and J. L. Patton, "A highly backdrivable, lightweight knee actuator for investigating gait in stroke," (in English), *IEEE Trans. Robot.*, vol. 25, no. 3, pp. 539–548, Jun. 2009.

[22] J. M. Caputo and S. H. Collins, "Prosthetic ankle push-off work reduces metabolic rate but not collision work in non-amputee walking," *Sci. Rep.*, vol. 4, no. 1, pp. 1–9, 2014.

[23] G. Lee, Y. Ding, I. G. Bujanda, N. Karavas, Y. M. Zhou, and C. J. Walsh, "Improved assistive profile tracking of soft exosuits for walking and jogging with off-board actuation," in *Proc. IEEE/RSJ Int. Conf. Intell. Robots Syst.*, 2017, pp. 1699–1706.

[24] X. Yang *et al.*, "Spine-inspired continuum soft exoskeleton for stoop lifting assistance," *IEEE Robot. Autom. Lett.*, vol. 4, no. 4, pp. 4547–4554, Oct. 2019.

[25] B. Katz, J. Di Carlo, and S. Kim, "Mini cheetah: A platform for pushing the limits of dynamic quadruped control," in *Proc. IEEE Int. Conf. Robot. Autom.*, 2019, pp. 6295–6301.

[26] W. E. Woodson, B. Tillman, and P. Tillman, *Human Factors Design Handbook: Information and Guidelines for the Design of Systems, Facilities, Equipment, and Products for Human Use*. New York, NY, USA: McGraw-Hill, 1992.

[27] M. Grimmer and A. Seyfarth, "Mimicking human-like leg function in prosthetic limbs," in *Neuro-Robotics*, Berlin, Germany: Springer, 2014, pp. 105–155.

[28] K. Seo, J. Lee, and Y. J. Park, "Autonomous hip exoskeleton saves metabolic cost of walking uphill," in *Proc. IEEE Int. Conf. Rehabil. Robot.*, 2017, pp. 246–251.

[29] J. Lee, K. Seo, B. Lim, J. Jang, K. Kim, and H. Choi, "Effects of assistance timing on metabolic cost, assistance power, and gait parameters for a hip-type exoskeleton," in *Proc. IEEE Int. Conf. Rehabil. Robot.*, 2017, pp. 498–504.

[30] Y. Ding and H.-W. Park, "Design and experimental implementation of a quasi-direct-drive leg for optimized jumping," in *Proc. IEEE/RSJ Int. Conf. Intell. Robots Syst.*, 2017, pp. 300–305.

[31] H. Zhu, C. Nesler, N. Divekar, M. T. Ahmad, and R. D. Gregg, "Design and validation of a partial-assist knee orthosis with compact, backdrivable actuation," in *Proc. IEEE Int. Conf. Rehabil. Robot.*, 2019, pp. 917–924.

[32] J. Wang, X. Li, T.H. Huang, S. Yu, Y. Li, and H. Su, "Comfort-centered design of a lightweight and backdrivable knee exoskeleton," *IEEE Robot. Autom. Lett.*, vol. 3, no. 4, pp. 4265–4272, Oct. 2018.

[33] T. Reichert, T. Nussbaumer, and J. W. Kolar, "Torque scaling laws for interior and exterior rotor permanent magnet machines," *IEEE Int. Magnetics Conf.*, vol. 3, pp. 4–7, 2009.

[34] J. J. Lee *et al.*, "Comparison between concentrated and distributed winding in IPMSM for traction application," in *Proc. IEEE Int. Conf. Elect. Mach. Syst.*, 2010, pp. 1172–1174.

[35] J. Wolff, C. Parker, J. Borisoff, W. B. Mortenson, and J. Mattie, "A survey of stakeholder perspectives on exoskeleton technology," *J. Neuroengineering Rehabil.*, vol. 11, no. 1, 2014, pp. 169–178.

[36] D. J. Gonzalez and H. H. Asada, "Hybrid open-loop closed-loop control of coupled human–robot balance during assisted stance transition with extra robotic legs," *IEEE Robot. Autom. Lett.*, vol. 4, no. 2, pp. 1676–1683, Apr. 2019.

[37] J. C. Mcleod, S. J. Ward, and A. L. Hicks, "Evaluation of the Keeogo Dermoskeleton," *Disability Rehabil., Assistive Technol.*, vol. 14, no. 5, pp. 503–512, Apr. 2019.

[38] H. L. Bartlett, B. E. Lawson, and M. Goldfarb, "Optimal transmission ratio selection for electric motor driven actuators with known output torque and motion trajectories," *J. Dyn. Syst., Meas., Control*, vol. 139, no. 10, 2017, Art. no. 101013.

[39] J. Yang *et al.*, "Machine learning based adaptive gait phase estimation using inertial measurement sensors," in *Des. Medi. Devices Conf.*, Minneapolis, USA, ASME Digital Collection, V001T09A010, 2019.

[40] A. S. McIntosh, K. T. Beatty, L. N. Dwan, and D. R. Vickers, "Gait dynamics on an inclined walkway," *J. Biomechanics*, vol. 39, no. 13, pp. 2491–2502, 2006.